nature electronics

ARTICLES

https://doi.org/10.1038/s41928-020-0388-x

Solution-processed upconversion photodetectors based on quantum dots

Wenjia Zhou[1], Yuequn Shang[1], F. Pelayo García de Arquer[2], Kaimin Xu[1], Ruili Wang[1], Shaobo Luo[1], Xiongbin Xiao[1], Xiaoyu Zhou[3], Ruimin Huang[3], Edward H. Sargent[2] and Zhijun Ning[1]✉

Upconversion photodetectors convert photons from the infrared to the visible light spectrum and are of use in applications such as infrared detection and imaging. High-performance upconversion devices are, however, typically based on vacuum-deposited materials, which are expensive and require high operating voltages, which limits their implementation in flexible systems. Here we report solution-processed optical upconversion photodetectors with a high photon-to-photon conversion efficiency of 6.5% and a low turn-on voltage of 2.5 V. Our devices consist of a colloidal lead sulfide quantum dot layer for harvesting infrared light that is monolithically coupled to a cadmium selenide/zinc selenide quantum dot layer for visible-light emission. We optimized the charge-extraction layers in these devices by incorporating silver nanoparticles into the electron transport layers to enable carrier tunnelling. Our photodetectors exhibit a low dark current, high detectivity (6.4×10^{12} Jones) and millisecond response time, and are compatible with flexible substrates. We also show that the devices can be used for in vitro bioimaging.

Quantum dots (QDs) offer a narrow linewidth emission and tunable bandgap, and are thus of potential value in the development of quantum information and optoelectronic devices[1–3]. Colloidal QDs (CQDs), in particular, can be obtained by solution processing and are used in photovoltaics[4–9], light emission[10–14] and photodetection[15–20].

Upconversion photodetectors, which convert low-energy photons (infrared, for example) to higher energy photons (visible, for example), are of use in infrared imaging (Fig. 1), which is used in applications such as night vision, semiconductor wafer inspection, gesture recognition, three-dimensional imaging and bioimaging[21–25]. Most infrared photon upconversion devices, however, are based on vacuum or high-temperature deposition methods[22,24–33], which are not compatible with electronic materials such as silicon and limits their use in flexible electronics. Two-terminal upconversion photodetectors based on solution-processed materials have been developed, but require high turn-on voltages and offer low photon-to-photon (p–p) efficiencies (below 1.5%)[30,34].

In this article, we show that two-terminal, solution-processed infrared upconversion photodetectors with an overall p–p efficiency of 6.5% and low turn-on voltages of 2.5 V can be created by engineering the electron transport layer (ETL). The efficiency of our photodetectors is comparable to that of epitaxially grown semiconductors and represents a fivefold increase compared with the highest-gain monolithic infrared quantum dot upconverters reported to date. Moreover, the low turn-on voltages of the devices represent a reduction of more than twofold compared with those of previous quantum dot upconverters.

Our devices consist of a photodetector absorption layer (infrared) based on lead sulfide (PbS) QDs and stacked with a light-emitting diode (LED) layer (visible light) based on cadmium selenide/zinc selenide (CdSe/ZnS) QDs (Fig. 2a). To ensure that the photodetector layer can provide sufficient photocurrent to drive the LED layer, we optimized the carrier tunnelling by incorporating silver (Ag) nanoparticles into the charge-extraction layers of the photodetector. This approach results in an enhanced tunnelling and thus a high photocurrent under illumination, as well as a low dark current in the absence of incident photons. We also showed that the photodetectors can be integrated onto flexible substrates. To illustrate the potential of our photodetectors, we also built top-emitting devices for bioimaging.

Device fabrication and working mechanism

We designed the infrared photodetector to convert incident light of 1,600 nm into visible emitted light. Luminescent CdSe/ZnS QDs (photoluminescence quantum yield >80%) with emission at 525 nm were used as the active material for the LED (Fig. 2b)[35,36] and narrow-bandgap PbS QDs (300–1,600 nm), synthesized via the hot injection method, as the active sensitizing material in the photodetector (Fig. 2c)[7,9]. The PbS nanoparticles were uniformly dispersed with a diameter of approximately 6 nm. We also used zinc oxide (ZnO) with embedded Ag nanoparticles as the ETL[37] and poly-(*N*,*N*-bis(4-butylphenyl)-*N*,*N*-bis(phenyl) benzidine) (poly-TPD) as the hole transport layer (Fig. 2a). We embedded Ag nanoparticles within the ZnO ETL layer to promote the accumulation of photogenerated electrons under illumination, which can bend the valence band of the ZnO, as indicated by simulation using Solar Cell Capacitance Simulator (SCAPS)[38] (Supplementary Figs. 1 and 2), and therefore facilitate the tunnelling of holes from the indium-doped tin oxide (ITO) contact (Fig. 3a)[39,40]. This could, in principle, improve the photocurrent and enable photoconductive gain.

We investigated the role of Ag nanoparticles in the ETL of the photodiode. Energy-dispersive X-ray spectroscopy (EDS) in scanning electron microscopy (SEM) revealed the presence of Ag nanoparticles in the films, centred in the middle of the ETL

[1]School of Physical Science and Technology, ShanghaiTech University, Shanghai, China. [2]Department of Electrical and Computer Engineering, University of Toronto, Toronto, Ontario, Canada. [3]Shanghai Institute of Materia Medica, Chinese Academy of Sciences, Shanghai, China. ✉e-mail: ningzhj@shanghaitech.edu.cn

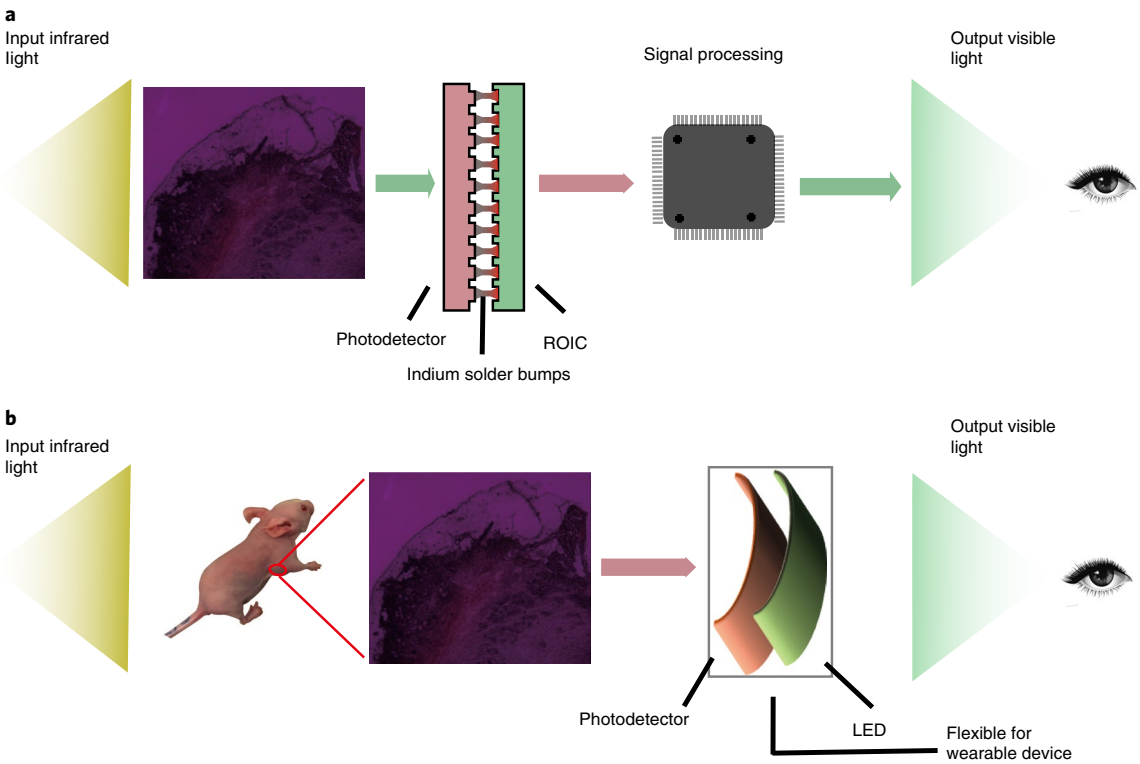

Fig. 1 | Infrared imaging using flexible upconversion devices. a,**b**, Traditional infrared imaging approach (**a**) versus the upconversion approach (**b**). The upconversion photodetector does not require a pixel connect process, such as indium bump bonding. ROIC, readout integrated circuit.

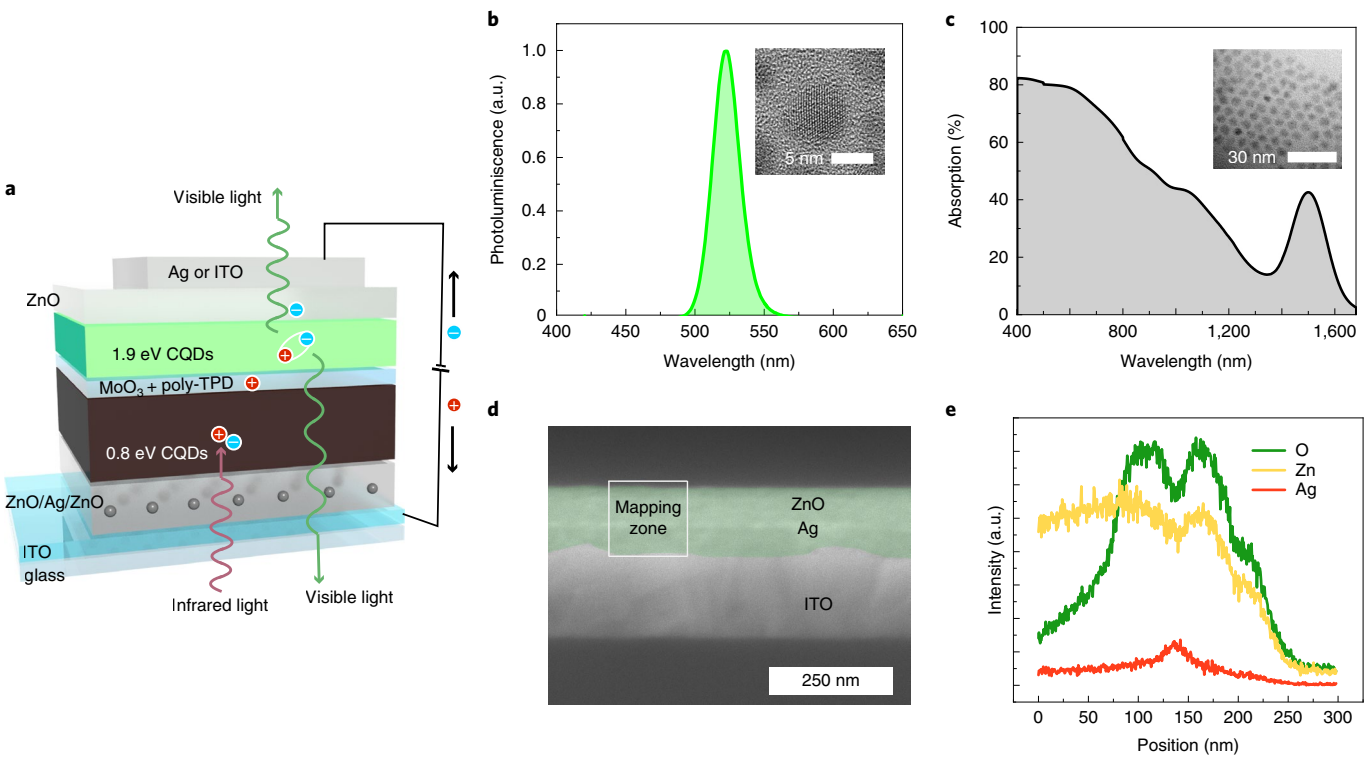

Fig. 2 | Structure and composition of upconversion devices herein. a, CQDs are used as the infrared sensitive layer and CdSe/ZnS core/shell QDs are used as the top visible light emission layer. **b**, PL spectra of CdSe/ZnS core/shell QDs, with the peak position at 525 nm. Inset: transmission electron microscopy (TEM) of CdSe/ZnS QDs. **c**, Absorbance of PbS QD thin films: the exciton peak position is at 1,500 nm. Inset: TEM of PbS QDs. **d**, Cross-sectional SEM image of the ZnO films with Ag nanoparticles. **e**, Cross-section EDS elemental line scan results of ZnO films with Ag nanoparticles. a.u., arbitrary units.

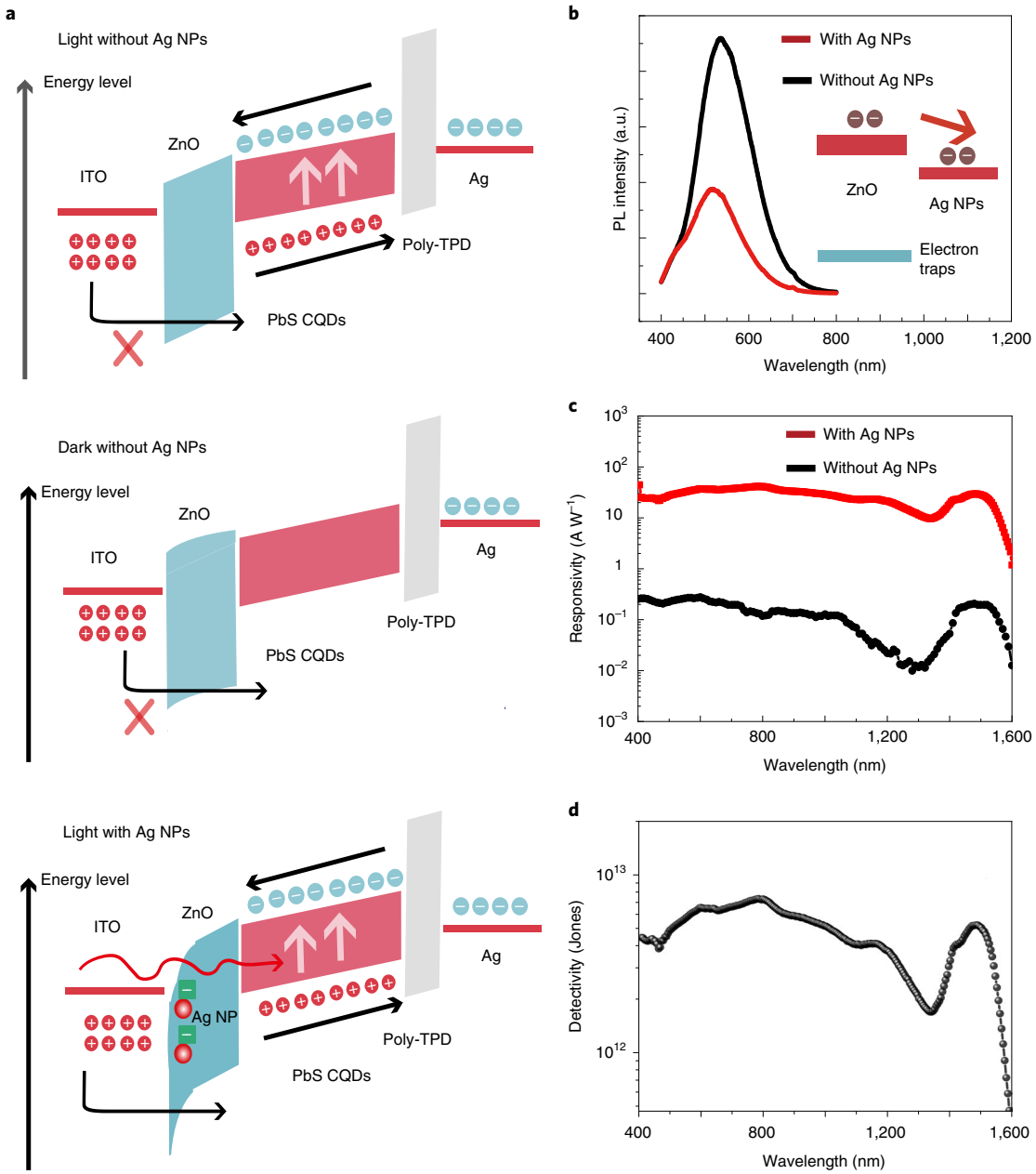

Fig. 3 | Operation of the photodetector. a, Energy band diagram of the photodetector with Ag nanoparticles in the ZnO film. Without Ag nanoparticles (top) or in the dark (middle), hole transfer from ITO to ZnO film is blocked by the energy level offset. Under illumination (bottom), holes tunnel into the ZnO film. **b**, PL spectra of ZnO films with and without Ag nanoparticles. The luminescence intensity is decreased with the inclusion of Ag nanoparticles. Inset: Ag nanoparticles that serve as electron traps in the ZnO films. **c**, Responsivities of PbS photodetectors with and without Ag nanoparticles in ZnO films under a −1 V bias. **d**, Detectivity of the photodetector with Ag nanoparticles in ZnO films under a −1 V bias.

(Fig. 2d,e, and Extended Data Fig. 1). To characterize any electron-accumulating role played by the Ag nanoparticles, we obtained the photoluminescence (PL) spectra of ZnO films with and without Ag nanoparticles (Fig. 3). Emission peaks at 530 nm were observed for each class of samples, whereas the PL intensity of the film with Ag nanoparticles was much lower. We ascribe this to electron transfer from ZnO to Ag nanoparticles, which reduced the density of charge carriers available for radiative recombination (inset of Fig. 3b).

To study charge transport within the ZnO:Ag composites, we fabricated ITO/ZnO/Al devices with and without Ag nanoparticles inside. Transient photocurrent traces of ZnO:Ag devices exhibit a longer temporal response compared to those of undoped ZnO devices, consistent with selective carrier trapping in the Ag nanoparticles (Supplementary Fig. 3)[39,40].

Upconversion performances

The responsivity of the resulting photodetector devices follows the absorption of the QDs, and exhibit a defined exciton peak at 1,500 nm. Under a reverse bias, devices exhibit gain, with a peak responsivity of >20 A W^{-1} in the short wave infrared and >60 A W^{-1} across the visible. Devices without Ag nanoparticles, however, display no gain and provide responsivities lower than 0.3 A W^{-1} (Fig. 3a,c).

The devices show typical diode characteristics in the dark and display a saturation current under a reverse bias (Supplementary Fig. 4). The magnitude of the dark current under a −1 V bias is below

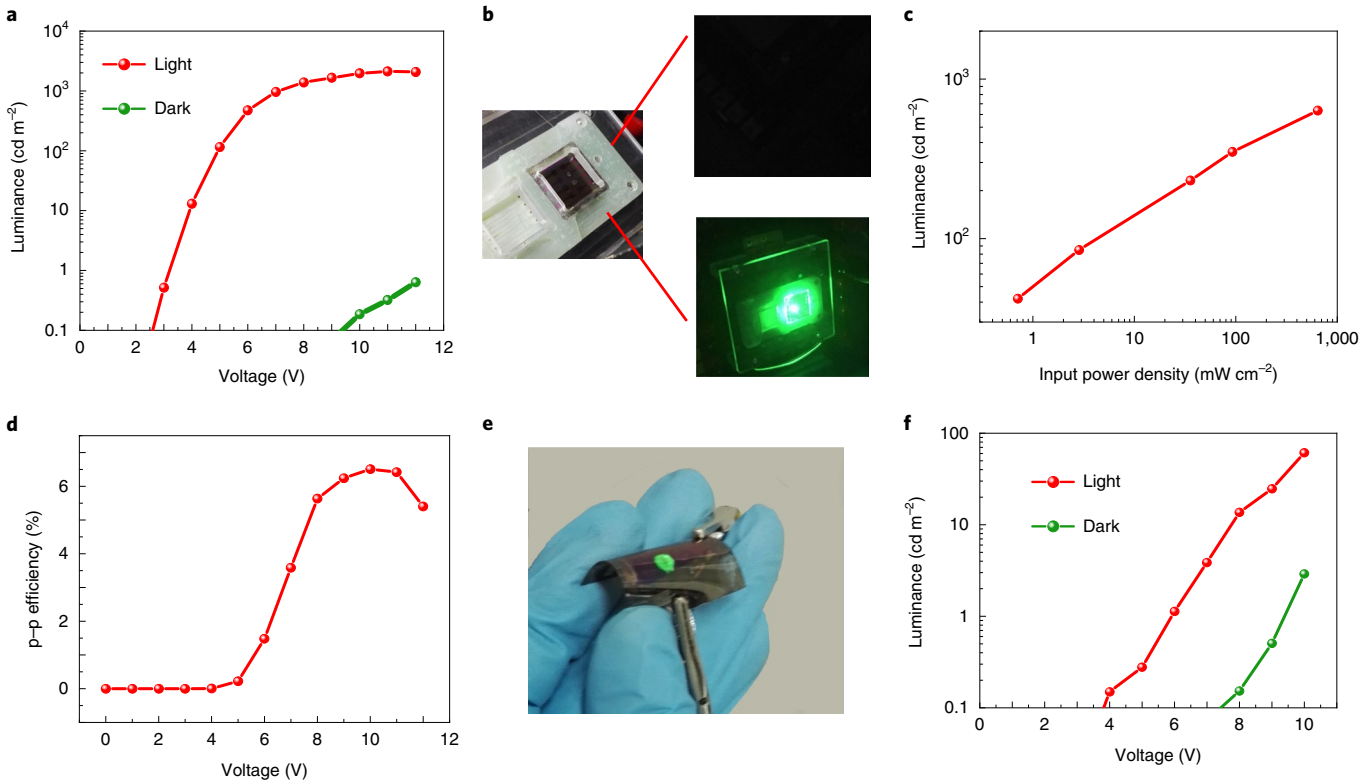

Fig. 4 | Characterization of solution-processed upconversion devices. a, Luminance–voltage characteristics of a device in dark versus light conditions. **b**, Photograph of a sample clamped in the measurement box (left), and images of a device (area of 0.05 cm^2) with (bottom) and without (top) infrared light (940 nm, 10 mW cm^{-2}). **c**, Infrared power dependence of the luminance of an upconversion device (940 nm at 6 V). A linear increase of current is observed with the increase of illumination intensity. **d**, Infrared to visible p–p characteristics of a flexible device when bent. **e**, Photograph of an operating flexible device when bent. **f**, Luminance–voltage characteristics of a flexible device when bent.

13 μA cm^{-2}, whereas the current increases dramatically under illumination. To characterize the sensitivity of the devices, we measured the specific detectivity (D^*):

$$D^* = \frac{\sqrt{AB}}{\mathrm{NEP}} \quad (1)$$

where A is the electrical device area and B is the electrical measurement bandwidth. Using a spectrum analyser, we obtained the noise equivalent power (NEP) from the noise current spectra under a −1 V reverse bias (Supplementary Fig. 5). At low frequencies, the noise current is dominated by flicker 1/f components. The resulting NEP reaches 3×10^{-14} W Hz$^{-1/2}$, which leads to a D^* of 6×10^{12} Jones at a frequency of 180 Hz (Fig. 3d). This is on a par with the best previously reported PbS-based infrared photodetectors of similar bandgap (Extended Data Fig. 2)[17,31,41,42,43,44].

We then sought to assess the time response of the photodetectors. The rise time from 10 to 90% and the fall time from 90 to 10% are 1 ms and 1.5 ms, respectively (Supplementary Fig. 4), compatible with imaging[17,41]. This response time is determined by the trap-related gain mechanism. The resulting combination of D^* and speed ranks among the best for infrared solution-processed photodetectors (Supplementary Fig. 4)[17,42–46].

A two-terminal upconversion photodetector was built first on a bottom-illumination structure, in which an LED is stacked on the top of the photodetector. Luminescent CdSe/ZnS QDs (photoluminescence quantum yield >80%) with emission at 525 nm were used as the active material for the LED[35,36]. To prevent interlayer disruption, we selected solvents for the fabrication of each layer. The low polarity solvent chlorobenzene was used for the fabrication of the intermediate poly-TPD layer (Supplementary Fig. 6) to prevent damage to the QD layer beneath. The use of octane (non-polar solvent) for the CdSe/ZnS QD layer avoided damage to the underlying poly-TPD layer (Supplementary Fig. 7). In contrast, solvents such as toluene partially dissolved the organic film, and the films fabricated using hexane showed a poor morphology. On top, a ZnO layer was fabricated using a polar solvent (ethanol), a strategy that avoided damage to the CQDs. Only through this approach were we able to build monolithically integrated solution-processed upconverters.

We then investigated the performance of the resultant upconversion photodetectors. Without infrared illumination, no light emission was observed even under a bias of 8 V (Fig. 4a). Under infrared illumination (940 nm, 10 mW cm^{-2}), a bright green light was observed over the device area (Fig. 4b). The dark current was below 0.7 mA cm^{-2} up to 5 V (Supplementary Fig. 8) and the current increased under increased near-infrared (NIR) illumination. In the absence of infrared light, the highest luminance was below 1 cd m^{-2} up to 12 V (Fig. 4a). Under NIR light, the optical upconversion devices reached a luminance of 2,100 cd m^{-2}, which provides an on–off ratio of 10^3. The turn-on voltage was 2.5 V (at 0.1 cd m^{-2}), facilitated by the high infrared photocurrent at low voltages. The upconversion photosignal increased monotonically over three decades of incident light density (Fig. 4c).

Photon-to-electron and electron-to-photon conversion efficiencies (Supplementary Fig. 8) are performance metrics for upconversion devices. We obtained a high photon-to-electron efficiency under low voltages that reaches 900%. The electron-to-photon

Table 1 | Performance of two-terminal upconversion devices

Material	Deposition method	Peak p–p efficiency (%)	Turn-on voltage (V)	Maximum wavelength (nm)	Reference
CQD + organic	Solution + vapour deposition	1.3	7	1,500	30
Organic + perovskite	Solution + vapour deposition	<1	3	1,000	34
Organic	Vapor deposition	2.7	2.7	1,000	32
Inorganic + organic	Vapor deposition	0.2	~4	1,500	22
Inorganic + organic	Vapor deposition	59	9	1,500	27
CQD	Solution	6.5	2.5	1,600	This work

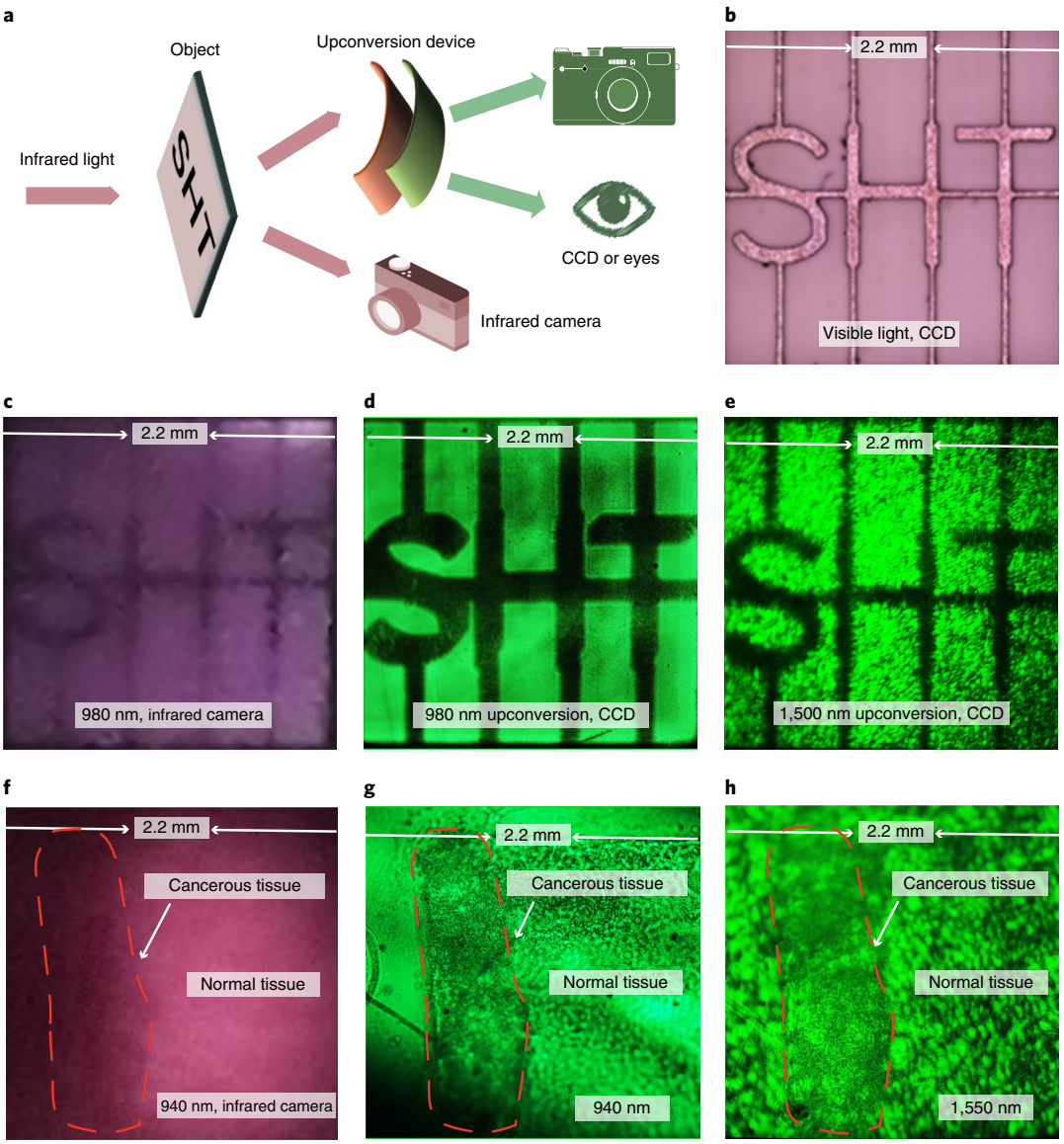

Fig. 5 | Applications of solution-processed upconversion devices. a, Schematic of an operating device under illumination using NIR light through the mask or tissue slides. **b**, Visible photograph of the mask patterned with the abbreviation for ShanghaiTech. **c**, Infrared photograph of the mask patterned with the same abbreviation. **d**, Photograph of the operating device with an illumination of 980-nm-NIR light through the mask. **e**, Photograph of the operating device with an illumination of 1,550-nm-NIR light through the mask. **f**, Infrared photograph of a tissue section (100 μm thick) from a mouse breast cancer sample under 940-nm-NIR light. **g**, Photograph of the operating device with the illumination of 940-nm-NIR light through the tissue section. **h**, Photograph of the operating device with the illumination of 1,550-nm-NIR light through the tissue section. CCD, charge-coupled device.

efficiency initially increases and then saturates at 7 V before decreasing. The highest electron-to-photon efficiency was 1%, a value lower than the typical efficiency of devices with a quantum dot LED only, which have efficiencies equal to about 5%. We attribute this to an imbalanced carrier injection into the light-emitting layer in the upconversion devices. In future, the addition

of carrier blocking layers could be used to the balance carrier injection[14].

We calculated the p–p upconversion efficiency for full monolithic devices using the equation:

$$\eta_{con} = \frac{\text{no. of emitted photons}}{\text{no. of extended incident photons}} = \frac{\int \frac{I_{photons}\lambda}{R_\lambda hc} d\lambda}{\frac{\lambda_{IR} P_{IR}}{hc}} \quad (2)$$

where $I_{photons}(\lambda)$ and $R(\lambda)$ are the photocurrent and photoresponsivity, respectively, of the photodetector in the instrument that collects the emitted visible photons, and λ_{IR} and P_{IR} are the wavelength and the incident infrared power, respectively (Fig. 4d). Under illuminance using 940 nm light, the maximum p–p conversion reaches 6.5%, comparable to the value reported for devices based on InGaAs photodetectors. This is the highest value reported for QD-based upconversion photodetectors based on two-terminal structures. Three-terminal structures have the potential to improve the p–p efficiency, but will complicate the device integration.

The devices achieve the longest response wavelength and the lowest turn-on voltage among the two-terminal infrared upconversion devices (Table 1). The combination of these advancements opens the possibility to fabricate flexible upconversion devices.

We fabricated prototype upconversion photodetectors employing an ITO/polyethylene terephthalate substrate to replace ITO/glass[47,48], which enabled operation on flexible substrates (Fig. 4e). Under considerable bending (radius of curvature 12 mm), the devices showed an efficient infrared upconversion. The luminance of the flexible upconversion photodetector under infrared light was ~61 cd m^{-2} (Fig. 4f), whereas only an extremely weak light emission could be detected under unilluminated conditions.

To avoid reabsorption of the emitted light by the QDs, we fabricated top-emitting upconversion devices in which ITO was used as a transparent top electrode. We achieved an overall p–p efficiency of 5.4% (Supplementary Fig. 9).

To demonstrate colour-tuning capability, we also built red-emitting devices (Supplementary Fig. 10). The p–p efficiency in this case is smaller compared to green LEDs and more optimization is needed to increase performance further.

Bioimaging application

To assess the imaging capability of the infrared-to-visible films, we placed a mask (Fig. 5a,b) in front of the film illuminated using infrared light (980 or 1,550 nm) and characterized the visible emission profile. The imaged shape is readily identified (Fig. 5d,e), which is comparable to the photograph taken using an infrared camera (Fig. 5c). The spatial resolution exceeds 16 line pairs mm^{-1}, as measured with the aid of a resolution test target (Supplementary Fig. 11).

To demonstrate upconversion devices in bioimaging applications, we illuminated a tissue section (100 µm) from a mouse breast cancer sample on a glass slide (Fig. 5f and Supplementary Fig. 12) using 940 or 1,550 nm infrared light. The higher cell density led to a weaker visible emission (Fig. 5g,h). Infrared light at these wavelengths resides within the tissue transparency window, which highlights the potential of this upconversion photodetector platform for in vivo health monitoring.

Conclusions

We fabricated flexible solution-processed upconversion photodetectors based on CQDs with a broadband response from 400 to 1,600 nm (near infrared into short-wave infrared). By adding Ag nanoparticles into the ZnO charge transport layers, our photodetectors exhibit a high photocurrent when illuminated and a low dark current operation under dark conditions, which results in a high photon-to-electron conversion efficiency and a low turn-on voltage of 2.5 V. In particular, the maximum p–p conversion efficiency is 6.5% for the bottom-emitting devices and 5.4% for the top-emitting devices. The specific detectivity of the devices reaches around 6.4×10^{12} Jones with around a millisecond response time. We also developed a flexible upconversion device, and a top-emitting upconversion device that could be used for bioimaging.

Methods

Material synthesis. PbS colloidal nanocrystals were synthesized based on the protocols reported by Sargent and co-workers[8]. Lead oxide (Aladdin, 99.99%) was dissolved in oleic acid (Aladdin, AR, 80–90%) and heated under vacuum at 95 °C for 16 h. The concentration of Pb in oleic acid was 1.346 M, achieved by dissolving 0.9 g (4.04 mmol) of lead oxide in 3 ml of oleic acid. Octadecene (ODE; 6 ml) (Aladdin, 90%) was added as the dilution solvent. After 16 h, an additional 20 ml of ODE were added for further dilution. Hexamethyldisilathiane (TMS; 420 µl (2.02 mmol)) (Sigma-Aldrich) was dissolved in 20 ml of ODE to form a 0.101 M solution. The TMS solution was then injected into lead oleate solution under vigorous stirring at 122 °C. After 30 s, the heating jacket was removed quickly and the mixed solution was cooled using an ice bath. When this reached room temperature, the nanocrystals were isolated by adding 60 ml of acetone (Sinopharm, AR). The nanocrystals were purified by dispersing in toluene (General-reagent, AR) and reprecipitated using acetone/hexane (General-reagent, AR) (1:1 volume ratio) and then re-dissolved in anhydrous toluene. The solution was washed with acetone/hexane three times before final dispersal in octane (Aladdin, AR, 96%) (50 mg ml^{-1}).

CdSe/ZnS QDs were prepared as follows: 0.2 mmol of cadmium oxide, 4 mmol of zinc acetate and 5 ml of oleic acid were placed in a 50 ml flask and heated to 150 °C under degassing, followed by a high-purity N_2 gas for 30 min. ODE (15 ml) was added to the flask and the temperature was increased to 310 °C. A stock solution that contained 0.4 mmol of selenium powder and 3.2 mmol of sulfur powder in 2 ml of trioctylphosphine was quickly injected into the flask. The reaction temperature was maintained at 300 °C for 10 min and then cooled to room temperature.

The resulting QD solution was repeatedly purified with a solvent combination of *n*-hexane and anhydrous ethanol (1:4 v/v) by centrifugation (10,000 r.p.m. for 10 min). Finally, the purified QDs were dispersed in octane to form a solution of 15 mg ml^{-1} accurately.

The ZnO nanoparticle solution was prepared based on the work of Waldo et al.[37]. ZnO nanoparticles were synthesized as follows: 2.96 g of zinc acetate dehydrate (Alfa, 98%) were dissolved in 125 ml of methanol at 60 °C, followed by the addition of a solution that contained 1.518 g of KOH (Adamas, 85%) dissolved in 65 ml of methanol for 10 min under vigorous stirring. After 2 h of heating and stirring, the heater and stirrer were removed and the nanoparticles were allowed to precipitate at room temperature overnight. The precipitate and solution were separated by centrifugation. The precipitate was subsequently washed with 50 ml of methanol twice. It was the dispersed in 20 ml of a mixed solvent that consisted of chloroform (General-reagent, AR, 99%) and methanol (Sinopharm, AR, 99.5%) in equal volume.

Top ZnO nanoparticles were synthesized using a solution–precipitation process. Briefly, zinc acetate dihydrate (1.308 g, 6 mmol) was dissolved in 60 ml of DMSO to form a colourless transparent solution. Then, tetramethylammonium hydroxide pentahydrate (1.68 g, 9 mmol) mixed with 20 ml of ethanol was added dropwise into the zinc acetate solution and stirred for 4 h in ambient air. The ZnO nanoparticles were centrifuged and washed with ethyl acetate twice, and 80 µl of ethanolamine was added during the second cleaning process. Last, ZnO nanoparticles were dispersed in ethanol to form a transparent solution with a concentration of 30 mg ml^{-1}.

Ag nanocrystals were synthesized by the reaction of $AgNO_3$ and oleylamine in toluene. $AgNO_3$ (1 mmol) and oleylamine (4 ml) were added into 100 ml of toluene. The solution was heated to 110 °C under a N_2 flow and stirred for 6 h. After the reaction, the solution was cooled to room temperature. Anhydrous ethanol (100 ml) was poured into the solution to precipitate the Ag NPs. The suspension was centrifuged at 6,000 r.p.m. for 5 min. The supernatant was discarded. The precipitate was washed with toluene and ethanol twice, then dried and dissolved in toluene (25 mg ml^{-1}).

Fabrication of infrared CQD photodetectors. Prepatterned ITO glass was cleaned using Triton X-100 (Sigma-Aldrich), deionized water, isopropyl alcohol (General-reagent, AR, 99.7%) and deionized water in order in an ultrasonic bath for 30 min each, followed by plasma treatment for 10 min. ZnO nanoparticles were spin coated on top of the plasma-treated ITO glass in air at 6,000 r.p.m. for 30 s, followed by heat treatment at 70 °C for 10 min. Ag nanoparticles (5 mg ml^{-1}) dissolved in octane were spin coated on the first ZnO layer (3,000 r.p.m., 30 s) followed by heat treatment at 70 °C for 10 min. Then, another ZnO layer was spin coated on the Ag nanoparticle layer, followed by heat treatment at 70 °C for 10 min. The substrates were then transferred to a N_2-filled glove box. The PbS layer was deposited via layer-by-layer spin coating. For each layer, two drops of PbS solution were spin cast on to the ZnO substrate at 2,500 r.p.m. for 10 s. A tetrabutylammonium iodide solution (10 mg ml^{-1} in methanol) was then dropped on to the film and left for 30 s, followed by two rinse–spin steps using methanol. Then, a layer of 1,2-ethanedithiol in acetonitrile solution (0.02 vol%) was used. An electron-blocking layer was spin coated on to the final film at 4,000 r.p.m. for 60 s using a poly-TPD solution (8 mg ml^{-1} dissolved

in chlorobenzene), followed by heat treatment at 80 °C for 10 min. For the top electrode, 100 nm of Ag was deposited using an Angstrom Engineering deposition system with a deposition rate of 0.2 Å s^{-1} for the first 20 nm and 1 Å s^{-1} for the last 80 nm. A shadow mask was used to define the illuminated area as 0.05 cm^2. The electrical area of the device was defined to be 0.065 cm^2 by the intersection of the bottom ITO substrate and the top electrode.

Fabrication of upconversion devices. To fabricate upconversion devices, we incorporated a quantum dot LED onto the infrared photodetector prior to electrode deposition. Before the deposition of the poly-TPD layer, a MoO_x precursor was spin cast at 3,000 r.p.m. and annealed at 80 °C for 10 min. After the deposition of the poly-TPD layer, CdSe/ZnS core/shell QDs dissolved in octane (10 mg ml^{-1}) were spin coated at 2,000 r.p.m. for 30 s, followed by heat treatment at 80 °C for 10 min. The ZnO film was spin cast at 2,000 r.p.m. for 30 s, followed by heat treatment at 80 °C for 10 min. Finally, 100 nm Ag or 140 nm ITO were deposited using an Angstrom Engineering deposition system.

Material characterization. PL signals were recorded using a spectrofluorometer (Fluorolog; HORIBA FL-3) and analysed using FluorEssence software. The absorption spectra were measured using an ultraviolet–visible spectrophotometer (Agilent Cary 5000). TEM and high-resolution TEM images were acquired using a JEOL 2100Plus TEM at an acceleration voltage of 200 kV. SEM images were obtained using a JSM 7800F SEM/EDS.

Device characterization. Current–voltage characteristics of the photodetector and upconversion devices were recorded using a Keithley 2400 source meter. Spectral responsivity was measured using a commercial system (Solar Cell Scan100, Beijing Zolix Instruments Co., Ltd). The cells were subjected to monochromatic illumination (150 W Xe lamp and Br tungsten lamp passing through a monochromator and appropriate filters). The light intensity was calibrated using standard Si and Ge photodetectors (QE-B3/S1337-1010BQ, Zolix). The light beam was chopped at 180 Hz and the response of devices was acquired using a Stanford Research SR830 lock-in amplifier. For the response speed measurement, a 640 nm laser (Coherent, OBIS) triggered by a waveform generator (Tektronix, AFG2021) with different modulation frequencies was used as the light source and the signals were recorded using an oscilloscope (Tektronix, MDO3034) with an input impedance of 50 Ω. For the characterization of upconversion devices, a 940 nm LED diode was used as the infrared light source and the intensity of light was controlled using neutral density filters. For the luminance–voltage measurements, a PR 655 (Photo Research) spectrometer was used. The electroluminescence characteristics of the upconversion devices were cross-checked using a system that comprised a fibre integration sphere (FOIS-1) coupled with a QE650pro spectrometer for light-output measurements.

Mouse breast tissue. All the animal experiments were approved by the Institutional Animal Care and Use Committee of Shanghai Institute of Materia Medica, Chinese Academy of Sciences. 4T1 mouse breast cancer cells (1×10^6) were suspended with 100 µl of 50% Matrigel (BD Bioscience) in PBS and injected subcutaneously in 5-week-old female BALB/c nude mice ($n = 5$; Beijing Vital River Laboratory Animal Technology). After 1 week, tumour samples that contained the tumour margins were harvested, fixed in 4% paraformaldehyde at 4 °C overnight and then transferred into 30% sucrose at 4 °C for 72 h. Samples were finally embedded in Tissue Freezing Medium (Leica Biosystems) and cut into 100-µm-thick sections for further imaging studies.

Data availability

The data that support the plots within this paper and other findings of this study are available from the corresponding author upon reasonable request.

Received: 22 December 2018; Accepted: 26 February 2020;
Published online: 30 March 2020

References

1. Imamoglu, A. et al. Quantum information processing using quantum dot spins and cavity QED. *Phys. Rev. Lett.* **83**, 4204–4207 (1999).
2. Hadfield, R. H. Single-photon detectors for optical quantum information applications. *Nat. Photon.* **3**, 696–705 (2009).
3. Bayer, M. et al. Coupling and entangling of quantum states in quantum dot molecules. *Science* **291**, 451–453 (2001).
4. Liu, M. et al. Hybrid organic–inorganic inks flatten the energy landscape in colloidal quantum dot solids. *Nat. Mater.* **16**, 258–263 (2016).
5. Sargent, E. H. Colloidal quantum dot solar cells. *Nat. Photon.* **6**, 133–135 (2012).
6. Sargent, E. H. Infrared photovoltaics made by solution processing. *Nat. Photon.* **3**, 325–331 (2009).
7. Ning, Z. et al. Air-stable n-type colloidal quantum dot solids. *Nat. Mater.* **13**, 822–828 (2014).
8. Ning, Z. et al. Graded doping for enhanced colloidal quantum dot photovoltaics. *Adv. Mater.* **25**, 1719–1723 (2013).
9. Wang, R. et al. Colloidal quantum dot ligand engineering for high performance solar cells. *Energy Environ. Sci.* **9**, 1130–1143 (2016).
10. Anikeeva, P. O., Halpert, J. E., Bawendi, M. G. & Bulović, V. Quantum dot light-emitting devices with electroluminescence tunable over the entire visible spectrum. *Nano Lett.* **9**, 2532–2536 (2009).
11. Caruge, J. M., Halpert, J. E., Wood, V., Bulović, V. & Bawendi, M. G. Colloidal quantum-dot light-emitting diodes with metal–oxide charge transport layers. *Nat. Photon.* **2**, 247–250 (2008).
12. Kwak, J. et al. Bright and efficient full-color colloidal quantum dot light-emitting diodes using an inverted device structure. *Nano Lett.* **12**, 2362–2366 (2012).
13. Mashford, B. S. et al. High-efficiency quantum-dot light-emitting devices with enhanced charge injection. *Nat. Photon.* **7**, 407–412 (2013).
14. Dai, X. et al. Solution-processed, high-performance light-emitting diodes based on quantum dots. *Nature* **515**, 96–99 (2014).
15. Adinolfi, V. et al. Photojunction field-effect transistor based on a colloidal quantum dot absorber channel layer. *ACS Nano* **9**, 356–362 (2015).
16. Zheng, L. et al. Ambipolar graphene–quantum dot phototransistors with CMOS compatibility. *Adv. Opt. Mater.* **6**, 1800985 (2018).
17. Konstantatos, G. et al. Ultrasensitive solution-cast quantum dot photodetectors. *Nature* **442**, 180–183 (2006).
18. Konstantatos, G. & Sargent, E. H. Nanostructured materials for photon detection. *Nat. Nanotechnol.* **5**, 391–400 (2010).
19. García de Arquer, F. P., Armin, A., Meredith, P. & Sargent, E. H. Solution-processed semiconductors for next-generation photodetectors. *Nat. Rev. Mater.* **2**, 16100 (2017).
20. McDonald, S. A. et al. Solution-processed PbS quantum dot infrared photodetectors and photovoltaics. *Nat. Mater.* **4**, 138–142 (2005).
21. Ban, D. et al. Near-infrared to visible light optical upconversion by direct tandem integration of organic light-emitting diode and inorganic photodetector. *Appl. Phys. Lett.* **90**, 093108 (2007).
22. Chen, J. et al. Hybrid organic/Inorganic optical up-converter for pixel-less near-infrared imaging. *Adv. Mater.* **24**, 3138–3142 (2012).
23. Dam, J. S., Tidemand-Lichtenberg, P. & Pedersen, C. Room-temperature mid-infrared single-photon spectral imaging. *Nat. Photon.* **6**, 788–793 (2012).
24. Lu, J., Zheng, Y., Chen, Z., Xiao, L. & Gong, Q. Optical upconversion devices based on photosensitizer-doped organic light-emitting diodes. *Appl. Phys. Lett.* **91**, 201107 (2007).
25. Yu, H. et al. High-gain infrared-to-visible upconversion light-emitting phototransistors. *Nat. Photon.* **10**, 129–134 (2016).
26. Chen, J. et al. Enhanced efficiency in near-infrared inorganic/organic hybrid optical upconverter with an embedded mirror. *J. Appl. Phys.* **103**, 103112 (2008).
27. Chen, J. et al. Near-infrared inorganic/organic optical upconverter with an external power efficiency of >100%. *Adv. Mater.* **22**, 4900–4904 (2010).
28. Chu, X. et al. Improved efficiency of organic/inorganic hybrid near-infrared light upconverter by device optimization. *ACS Appl. Mater. Interfaces* **4**, 4976–4980 (2012).
29. Chen, J. et al. Near-infrared optical upconverter based on i-$In_{0.53}Ga_{0.47}As/C_{60}$ photovoltaic heterojunction. *Electron. Lett.* **45**, 753–755 (2009).
30. Kim, D. Y. et al. PbSe nanocrystal-based infrared-to-visible up-conversion device. *Nano Lett.* **11**, 2109–2113 (2011).
31. Manders, J. R. et al. Low-noise multispectral photodetectors made from all solution-processed inorganic semiconductors. *Adv. Funct. Mater.* **24**, 7205–7210 (2014).
32. Kim, D. Y., Song, D. W., Chopra, N., De Somer, P. & So, F. Organic infrared upconversion device. *Adv. Mater.* **22**, 2260–2263 (2010).
33. Luo, H., Ban, D., Liu, H. C., Wasilewski, Z. R. & Buchanan, M. Optical upconverter with integrated heterojunction phototransistor and light-emitting diode. *Appl. Phys. Lett.* **88**, 073501 (2006).
34. Li, N., Lau, Y. S., Xiao, Z., Ding, L. & Zhu, F. NIR to visible light upconversion devices comprising an NIR charge generation layer and a perovskite emitter. *Adv. Opt. Mater.* **6**, 1801084 (2018).
35. Kang, B.-H. et al. Efficient exciton generation in atomic passivated CdSe/ZnS quantum dots light-emitting devices. *Sci. Rep.* **6**, 34659 (2016).
36. Choi, M. K. et al. Wearable red–green–blue quantum dot light-emitting diode array using high-resolution intaglio transfer printing. *Nat. Commun.* **6**, 7149 (2015).
37. Wang, R. et al. Highly efficient inverted structural quantum dot solar cells. *Adv. Mater.* **30**, 1704882 (2018).
38. Burgelman, M., Nollet, P. & Degrave, S. Modelling polycrystalline semiconductor solar cells. *Thin Solid Films* **361–362**, 527–532 (2000).
39. Guo, F. et al. A nanocomposite ultraviolet photodetector based on interfacial trap-controlled charge injection. *Nat. Nanotechnol.* **7**, 798–802 (2012).
40. Miao, J. & Zhang, F. Recent progress on photomultiplication type organic photodetectors. *Laser Photon. Rev.* **13**, 1800204 (2019).
41. Clifford, J. P. et al. Fast, sensitive and spectrally tuneable colloidal-quantum-dot photodetectors. *Nat. Nanotechnol.* **4**, 40–44 (2008).

42. Konstantatos, G. et al. Hybrid graphene–quantum dot phototransistors with ultrahigh gain. *Nat. Nanotechnol.* **7**, 363–368 (2012).
43. Wei, Y. et al. Hybrid organic/PbS quantum dot bilayer photodetector with low dark current and high detectivity. *Adv. Func. Mater.* **28**, 1706690 (2018).
44. Adinolfi, V. & Sargent, E. H. Photovoltage field-effect transistors. *Nature* **542**, 324–327 (2017).
45. Nikitskiy, I. et al. Integrating an electrically active colloidal quantum dot photodiode with a graphene phototransistor. *Nat. Commun.* **7**, 11954 (2016).
46. Hamers, R. J. Flexible electronic futures. *Nature* **412**, 489–490 (2001).
47. Russo, A. et al. Pen-on-paper flexible electronics. *Adv. Mater.* **23**, 3426–3430 (2011).
48. Yu, Z. et al. Highly flexible silver nanowire electrodes for shape-memory polymer light-emitting diodes. *Adv. Mater.* **23**, 664–668 (2011).

Acknowledgements

We acknowledge financial support from the National Key Research and Development Program of China (under Grant no. 2016YFA0204000), National Natural Science Foundation of China (61935016, U1632118 and 21571129), Shanghai Tech start-up funding, 1000 Young Talent program and the Science and Technology Commission of Shanghai Municipality (16JC1402100 and 16520720700). We thank the support from Analytical Instrumentation Center (#SPST-AIC10112914), SPST, ShanghaiTech University. We thank X. Wang at Alberta University for helpful discussions. We also thank B. Chen and his group members for their help of measuing the noise of photodetector.

Author contributions

W.Z. and Z.N. conceived the idea and designed the experiments. K.X., R.W. and Y.S. synthesized the QDs. W.Z., S.L., X.X. and Y.S. fabricated and measured the devices. W.Z. performed theoretical modelling. X.Z. and R.H. performed the tumour growth in mice experiments. W.Z. and F.P.G.A. carried out the data analysis. W.Z., Z.N., F.P.G.A. and E.H.S. co-wrote the manuscript. All the authors contributed to the editing of the manuscript.

Competing interests

The authors declare no competing interests.

Additional information

Extended data is available for this paper at https://doi.org/10.1038/s41928-020-0388-x.

Supplementary information is available for this paper at https://doi.org/10.1038/s41928-020-0388-x.

Correspondence and requests for materials should be addressed to Z.N.

Reprints and permissions information is available at www.nature.com/reprints.

Publisher's note Springer Nature remains neutral with regard to jurisdictional claims in published maps and institutional affiliations.

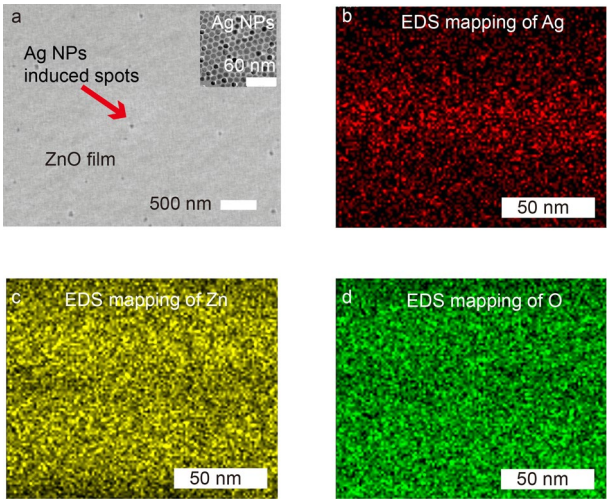

Extended Data Fig. 1 | Characterization of Ag nanoparticles in ZnO films. Characterization of Ag nanoparticles in ZnO films. (**a**) SEM image of the ZnO surface. (**b**)EDS elemental mapping images of the cross section of the ZnO films with Ag nanoparticles for Ag element. (**c**) EDS elemental mapping images of the cross section of the ZnO films with Ag nanoparticles for Zn element. (**d**) EDS elemental mapping images of the cross section of the ZnO films with Ag nanoparticles for O element.

Comparison of the performance of the photodetectors

Material	Device structure	Gain	Detectivity (Jones)	Bandwidth	Reference
PbS QDs	photodiode	80	6.4×10^{12}	1000 Hz	Our work
PbS QDs	photodiode	1	1×10^{12}	10^5 Hz	Ref. 41
PbS QDs	photoconductor	$>10^3$	1.8×10^{13}	18 Hz	Ref. 17
PbS QDs/Si	photovoltage Field effect transistor	$>10^4$	1.8×10^{12}	10^5 Hz	Ref. 44
PbS QDs	photodiode	1	1.1×10^{12}	36000Hz	Ref. 31
PbS QDs/organic	field effect transistor	3	1.12×10^{13}	3	Ref. 43
PbS QDs/graphene	field effect transistor	10^7	7×10^{13}	10 Hz	Ref. 42

Extended Data Fig. 2 | Comparison of the performance of the photodetectors. Comparison of the performance of the photodetectors.